This paper appears in IEEE Transactions on Medical Robotics and Bionics, 2022.
https://doi.org/10.1109/TMRB.2022.3214439

A Model-Based Multi-Point Tissue Manipulation for Enhancing Breast Brachytherapy

Mehrnoosh Afshar[1], Jay Carriere[2], *Member, IEEE*, Tyler Meyer[3], Ron Sloboda[4], Siraj Husain[3], Nawaid Usmani[4], and Mahdi Tavakoli[1], *Senior Member, IEEE*

***Abstract*—In surgical operations, tissue manipulation can be automated to reduce the surgeon's workload. This work addresses the application of tissue manipulation in breast brachytherapy, which involves manipulating an internal target inside the breast. Unassisted breast brachytherapy causes excessive target movement that reduces seed implantation accuracy. To address this target movement in breast brachytherapy, first, the internal target point will be manipulated accurately and then the brachytherapy needle will be inserted into the immobilized tissue. In this paper, a model-based tissue manipulation method is introduced. To simulate nonlinear large tissue deformation for the first time, a minimum-energy-based deformable tissue solver is utilized. Based on the theory of positive bases, the optimal number of actuators is determined to guarantee controllability of the internal target. A model predictive controller (MPC) is designed to implement multi-point tissue manipulation. A breast phantom is used to test the accuracy of the deformation model and the effectiveness of the proposed control method. The results show that the tissue deformation simulation error is 1.6 mm and the internal target can be regulated with negligible steady-state errors using an MPC controller.**

***Index Terms*—Breast brachytherapy, Soft tissue manipulation, Medical robotics, MPC controller, Tissue mechanical modelling**

I. INTRODUCTION

The use of semi-autonomous and robot-assisted surgeries enhances the accuracy and reliability of surgical procedures. Suturing, tissue manipulation, tremor reduction, and force control are among the low-level robotic operations that can be automated by robots. In percutaneous treatments, a needle is inserted into soft tissue to obtain tissue samples for biopsy purposes or to deliver drugs to specific organs. The low dose rate permanent seed implantation (LDR-PS) technique is a percutaneous procedure in which radioactive seeds are implanted in, or around, a cancerous tumor or seroma within the body. It is essential to have high accuracy regarding seed placement in order to achieve success with the treatment. A preoperative dosimetry analysis will determine seed distributions [1]. During brachytherapy treatments, two major phenomena, needle deflection during insertion and target movement, reduce accuracy in needle-tip placement and, therefore, implantation accuracy [1].

A. Clinical Need

During breast LDR-PS treatment, the target application of this study, breast tissue deforms easily and excessively. The pressure applied by the Ultrasound (US) probe, which is used to visualize the needle tip, deforms the breast as US probe moves over the breast surface (see Fig. 1). During the course of breast surgery, the target area may be dislocated up to 7 mm [2], [3]. The risk of cancer recurrence will increase if seeds are implanted off-target, as insufficient radiotherapy will be administered. Currently, the success of precise seed implantation in breast brachytherapy is highly dependent on the clinician's skill, since the clinician must track the 3D position of moving targets from 2D US images and manipulate the breast and needle simultaneously to ensure that seeds are planted at the desired location determined by the dosimetry analysis [4].

Immobilizing the breast with fixtures similar to those used during mammograms is one solution to resolve uncontrolled tissue deformation. However, this may adversely affect needle steering and cause patients pain. Therefore, uncontrolled tissue deformation must be addressed to have accurate seed implantation. In the literature, instead of controlling the tissue deformation, most studies focus on steering needles toward the targets particularly for prostate brachytherapy. In prostate brachytherapy, the insertion length is long enough to provide flexible needle with enough steerability in order to steer the needle toward the targets [5] and targets are not moving due to exessive tissue deformation. Breast brachytherapy, however, does not have a stationary target, nor is the insertion length sufficient to maneuver the conventional needle. With a 50 mm insertion length, the maximum needle tip deflection for 18G flexible needles used in the clinic (with a curvature radius of 650 mm) is less than 1 mm [6]. Therefore, standard beveled tips are not steerable enough to reach continuous moving targets in breast brachytherapy.

To overcome the challenges associated with tissue deformation and limited needle workspace in breast brachytherapy, it is suggested to control and manipulate tissue deformation. Through tissue deformation control, the internal target can either be moved toward the needle path or obstacles that block the needle path can be removed in place of steering the needle. Tissue manipulation can be an adjunct solution to the needle steering problem, especially when the target lays out of the reachable workspace of the beveled tip needle, which is a significant limitation in the case of breast brachytherapy. In this work, the focus is only on compressing the tissue because it is more practical. To the best of the authors' knowledge, tissue manipulation, particularly for percutaneous therapies, has not been extensively studied in the literature.

B. Related Studies

This subsection presents a review of deformable object manipulation studies in surgical applications and deformable object

This research was supported by the Canada Foundation for Innovation (CFI), the Natural Sciences and Engineering Research Council (NSERC) of Canada, the Canadian Institutes of Health Research (CIHR), and the Alberta Jobs, Economy and Innovation Ministry's Major Initiatives Fund to the Center for Autonomous Systems in Strengthening Future Communities.

[1]Mehrnoosh Afshar (Corresponding Author) and Mahdi Tavakoli are with the Department of Electrical and Computer Engineering, University of Alberta, AB, Canada T6G 1H9. afsharbo@ualberta.ca, mahdi.tavakoli@ualberta.ca

[2]Jay Carriere is with the Department of Electrical and Software Engineering, University of Calgary, AB, Canada, T2N 1N4. jay.carriere@ucalgary.ca

[3]Tyler Meyer and Siraj Husain are with the Division of Radiation Oncology, Tom Baker Cancer Centre, 331 29th Street NW, Calgary, Alberta T2N 4N2. tyler.meyer@albertahealthservices.ca, siraj.husain@albertahealthservices.ca.

[4]Ron Sloboda and Nawaid Usmani are with the Department of Oncology, Cross Cancer Institute, 11560 University Avenue, Edmonton, AB, Canada, T6G 1Z2. nawaid.usmani@albertahealthservices.ca, ron.sloboda@albertahealthservices.ca.

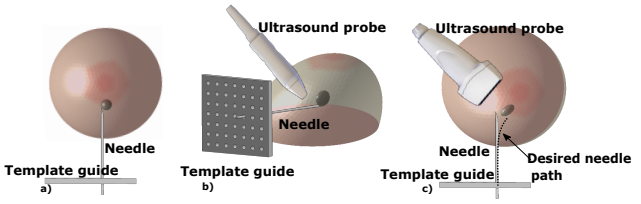

Fig. 1: Illustration of target movement in breast brachytherapy; a) ideal situation for the surgeon, b) and c) shows target deviation as a result of US pressure and the fact that the previous needle trajectory would not reach the target.

solvers for surgical applications to illustrate the contributions made by this work within the literature.

It is proposed to treat prostate cancer using a tissue manipulation procedure based on MSM models of 2D prostate motion [7]. However, its disadvantage is that the 2D linear model cannot address tissues' nonlinear and large deformations. In [8], the authors model a soft robot using linear FEM and obtain the control inputs using inverse FEM. A constraint-based inverse linear FEM simulation is used to steer a flexible needle inside a deformable tissue in [9]. It compensates for tissue movement by steering the needle via a robotic arm. The control of active tissue deformation is not the primary concern of [9]. The authors in [10] used a suction-based manipulator to manipulate the breast tissue from one point, reporting that the needle insertion accuracy was increased. In [11], a force-actuated position controller was implemented to manipulate breast tissue for biopsy treatment.The required forces for tissue manipulation were calculated based on real-time medical images. In both [11] and [10], no biomechanical model for tissue deformation prediction was used inside the control loop and a simple PID controller was developed. A visual servoing method was implemented by online Jacobin estimation to deform a soft object toward the desired position [12]. It has been attempted in several studies [13], [14] to learn the Jacobian between deformable object and robot manipulator from visual data in an online fashion.

While manipulating an interior point, it is impossible to receive visual feedback from the breast's internal parts. Accordingly, a biomechanical model must be incorporated into the structure of a model-based controller in order to establish a relationship between the movement of the internal target and the movement of the control points. This study highlights the lack of integration of a real-time nonlinear tissue solver into a control procedure for tissue manipulation (controlling tissue deformation).

Finite Element Methods (FEM) are widely used to simulate nonlinear and complicated mechanical behavior of tissue; however, they are computationally expensive at the moment to be used for real-time applications [15]. Numerous studies have applied model order reduction methods to FEM to enhance their computational performance. The reduced order model FEMs are obtained via a substantial pre-operative calculation [16]. Many studies simplified accurate models for a real-time solver in order to meet simulation speed requirements, however, this simplification decreases the model accuracy to some extent such as Mass Spring Models (MSMs) [17].

Position-based dynamics (PBD) methods has recently been utilized to develop surgical simulators [18].

A study by Tagliabue et al. [19] used PBD to predict the position of breast tumors in response to pressures from US scanning. Because the constraints in PBD are geometric, it does not reflect the mechanical characteristics of tissue. Therefore, the reported tumor localization error in [19] is extremely large for medical applications and it is about 5mm.

In [20], a generalization of the PBD method is presented that permits solving any nonlinear constraint. In this method, the alternating direction method of multiplier (ADMM) is used as the optimizer. As opposed to the usual optimizers, ADMM allows computations to be parallelized, making it a viable choice for simulations that occur in real-time.

C. Objective and Contributions

An innovative method is presented in this study to manipulate multiple points on the surface of tissue (in this case the breast) in order to steer an internal target to the desired location within the tissue. Before the needle is inserted, the target will be moved onto the needle path. As soon as the target has reached the desired location, the actuators will cease applying force to the tissue and a needle will be inserted to hit the target. This paper has the following contributing features:

1) Development of a fast tissue-deformation solver to model nonlinear hyperplastic behavior of the breast tissue. The main concept of the solver is to minimize the strain energy of tissue obtained from nonlinear material models. Implementation of the solver on a multi-core CPU or GPU provides the possibility of having a real-time solver suitable to be integrated into the control loop.
2) Showing the necessary and sufficient number of actuators that can guarantee the controllability of the internal target, where the internal target can be moved in an arbitrary manner, by using the theory of positive bases.
3) Defining a manipulability index and applying it to an analysis of the performance of different actuator configurations.
4) Developing a Model Predictive Controller (MPC) based upon the online linearization of tissue solver. The linear approximation is calculated analytically and relates the displacement of control points on the tissue boundary to the movement of the internal target.

The rest of the paper is organized as follows. The tissue solver and material model will be presented in Section II. A linear model derivation, controllability analysis, and MPC control method will be elaborated in Section III. In Section IV, the accuracy of the biomechanical model in deformation prediction and the performance of the control loop in steering the internal point of the tissue to the desired positions will be evaluated experimentally, and a conclusion in Section V will complete the paper.

II. Tissue Modelling

In this section, the mathematics of the minimum-energy-based method will be described, and how we have integrated our selected material model into the method will be explained.

A. Dynamics of Tissue Deformation

The object is discretized using elements (i.e., triangle for 2D and tetrahedral for 3D) and lumped masses are integrated on the ele-

ment's node. Each lumped mass is a DOF of the system. The dynamics of the system based on Newton's law in Eulerian coordinate is

$$\mathbf{M}\ddot{\mathbf{x}} = \mathbf{F}_{\text{int}} + \mathbf{F}_{\text{ext}} = \mathbf{f}(\mathbf{x},t) \tag{1}$$

Here, $\mathbf{M}$ is the matrix of lumped masses and $\mathbf{F}_{\text{int}}$ and $\mathbf{F}_{\text{ext}}$ are the internal and external forces acting on each DoF, respectively. In the context of continuum mechanics, internal forces are calculated as the gradient of strain energy function $\mathbf{F}_{\text{int}} = -\nabla \mathrm{U}(\mathbf{x})$. To solve the dynamic system in (1), it should be integrated through time. Considering the unconditional stability of implicit Euler scheme (backward Euler), it is usually selected to solve the dynamic systems. In this scheme, a system of implicit unknowns should be solved. The system of dynamic equations can be defined using the following set of equations

$$\begin{aligned} \mathbf{M}\mathbf{v}(t+\Delta t) &= \mathbf{M}\mathbf{v}(t) + \Delta t\, \mathbf{f}(\mathbf{v}(t+\Delta t), \mathbf{x}(t+\Delta t), t) \\ &= \mathbf{M}\mathbf{v}(t) + \mathbf{F}_{\mathbf{ext}}(t)\Delta t + \mathbf{F}_{\mathbf{int}}(t+\Delta t)\Delta t, \\ \mathbf{x}(t+\Delta t) &= \mathbf{x}(t) + \mathbf{v}(t+\Delta t)\Delta t \end{aligned} \tag{2}$$

where $\mathbf{v}(\mathbf{t})$ and $\mathbf{x}(\mathbf{t})$ are the velocity and displacement vectors of all DoFs. (2) is a set of high dimensional and highly nonlinear equations. One solution is to solve the set of equations using iterative methods such as Newton's method; however it can be reformulated to be solved as an optimization problem as suggested in [20]. The combinations of the set of equations in (2) leads to

$$\frac{1}{\Delta t^2}\mathbf{M}(\mathbf{x}(t+\Delta t) - \tilde{\mathbf{x}}(t+\Delta t)) = \mathbf{F}_{\mathbf{int}}(t+\Delta t) \tag{3}$$

where,

$$\tilde{\mathbf{x}}(t+\Delta t) = \mathbf{x}(t) + \mathbf{v}(t)\Delta t + \mathbf{M}^{-1}\mathbf{F}_{\mathbf{ext}}(t)\Delta t^2 \tag{4}$$

determines the position of lumped masses in the absence of internal forces. Considering the fact that $\mathbf{F}_{\mathbf{int}} = -\nabla \mathrm{U}(\mathbf{x})$, (3) can be reformulated to an optimization form based on the work in [20]

$$\mathbf{x}(t+\Delta t) = \underset{\mathbf{x}}{\operatorname{argmin}} \left(\frac{1}{2\Delta t^2} \|\mathbf{x} - \tilde{\mathbf{x}}(t+\Delta t)\|_{\mathbf{M}}^2 + U(\mathbf{x}) \right) \tag{5}$$

where $\|\mathbf{x}\|_{\mathrm{M}} = \sqrt{\mathbf{x}^T\mathbf{M}\mathbf{x}}$. Taking the gradient of (5) and equating it to zero leads to (3), therefore, the solution of (5) at each time step is the solution of (3). The DoF of dynamic system is equal to the number of nodes used to discretize the tissue domain multiplied by three in case of 3D simulation (DoF is denoted by $\mathbf{N}$); therefore, (5) is still a high dimension nonlinear optimization problem and it is not possible to be solved in an efficient time. To overcome this issue a solution, which is suggested in [20], is to use the alternating direction method of multipliers optimizer (ADMM) which in general is an optimizer for distributed systems.

B. ADMM Implementation For Tissue Deformation Dynamics

The strain energy deformation U is a function of gradient deformation matrix (will be explained thoroughly is Section II-C). A vector composed of the elements of gradient deformation matrices associated with mesh elements can be introduced into (5) as a new variable denoted by $\mathbf{z}$. The relationship of $\mathbf{z} = \mathbf{D}\mathbf{x}$ is satisfied between the variable $\mathbf{z}$ and $\mathbf{x}$ at each converged solution of (5). In fact, matrix $\mathbf{D}$ transforms $\mathbf{x}$ variables to the gradient deformation matrix space. Therefore, (5) can be reformulated as [20]

$$\begin{aligned} &\underset{\mathbf{x},\mathbf{z}}{\operatorname{argmin}} \left(\tfrac{1}{2\Delta t^2} \|\mathbf{x} - \tilde{\mathbf{x}}\|_{\mathbf{M}}^2 + \mathrm{U}(\mathbf{z}) \right) \\ &\text{s.t. } \mathbf{W}(\mathbf{D}\mathbf{x} - \mathbf{z}) = \mathbf{0} \end{aligned} \tag{6}$$

where $\mathbf{W}$ is a weighting matrix. By applying ADMM optimizer to (6), the update rules for the tissue deformation dynamics problem can be obtained as

$$\begin{aligned} \mathbf{x}^{n+1} &= \underset{\mathbf{x}}{\operatorname{argmin}} \left(\frac{1}{2\Delta t^2} \|\mathbf{x} - \tilde{\mathbf{x}}\|_M^2 + \frac{1}{2} \|\mathbf{W}(\mathbf{D}\mathbf{x} - \mathbf{z}^n + \mathbf{u}^n)\|^2 \right) \\ &= \left(\mathbf{M} + \Delta t^2 \mathbf{D}^T\mathbf{W}^T\mathbf{W}\mathbf{D}\right)^{-1} \left(\mathbf{M}\tilde{\mathbf{x}} + \Delta t^2 \mathbf{D}^T\mathbf{W}^T\mathbf{W}(\mathbf{z}^n - \mathbf{u}^n)\right) \end{aligned} \tag{7}$$

$$\mathbf{z}^{n+1} = \underset{\mathbf{z}}{\operatorname{argmin}} \left(\mathrm{U}(\mathbf{z}) + \frac{1}{2} \left\| \mathbf{W}\left(\mathbf{D}\mathbf{x}^{n+1} - \mathbf{z} + \mathbf{u}^n\right) \right\|^2 \right) \tag{8}$$

$$\mathbf{u}^{n+1} = \mathbf{u}^n + \mathbf{D}\mathbf{x}^{n+1} - \mathbf{z}^{n+1} \tag{9}$$

Matrices in (7) are fixed and can be precalculated, so the update rule for $\mathbf{x}$ variable is fast.

The tissue solver is parallelizable as (8) can be solved for each element separately; therefore, the procedure can be implemented in parallel on GPU or multi-core CPU. For each strain energy function associated with each element, the following optimization problem should be solved separately.

$$\begin{aligned} \mathbf{z}_i^{n+1} &= \underset{\mathbf{z}_i}{\operatorname{argmin}} \left(\mathrm{U}_i(\mathbf{z}_i) + \tfrac{1}{2} \left\| \mathbf{W}_i\left(\mathbf{D}_i\mathbf{x}^{n+1} - \mathbf{z}_i + \mathbf{u}_i^n\right) \right\|^2 \right) \\ \mathbf{u}_i^{n+1} &= \mathbf{u}_i^n + \mathbf{D}_i\mathbf{x}^{n+1} - \mathbf{z}_i^{n+1} \end{aligned} \tag{10}$$

Here, i refers to the element number, and $\mathbf{z_i}$ is a vector containing elements of the gradient deformation matrix associated with element i. After updating variable $\mathbf{z_i}$ and $\mathbf{u_i}$ associated with individual elements separately, the global vector of $\mathbf{z}$ and $\mathbf{u}$ are updated and used to update the position vector $\mathbf{x}$ using (7). For more details about the implementation of ADMM, an interested reader should refer to [20].

In the next section, we will explain how to choose $\mathrm{U}_i(\mathbf{z_i})$ to solve the optimization problem in (10).

C. Material Model

The strain energy density function quantifies the stored strain energy per volume of an element due to deformation. The strain energy density function, denoted by Ψ, is zero when there is no element deformation. Green-Saint-Venant strain tensor, $\mathbf{E}$, is a measure of strain of an element and is given by $\mathbf{E} = \frac{1}{2}(\mathbf{C} - \mathbf{I})$, where $\mathbf{I}$ is second-order identity tensor and $\mathbf{C}$ is the right Cauchy–Green deformation tensor, obtained by $\mathbf{C} = \mathbf{F}^\top\mathbf{F}$, and $\mathbf{F}$ is the deformation gradient matrix, calculated by

$$\mathbf{F} = \frac{\partial \mathbf{x}}{\partial \mathbf{X}} \tag{11}$$

where $\mathbf{x}$ is the current position of element's nodes (i.e., deformed configuration) and $\mathbf{X}$ is the position of element's nodes in the reference configuration (i.e., undeformed configuration). For tetrahedral element (i.e., a four node element) $\mathbf{F}$ can be obtained using $\mathbf{F} = \mathbf{N}_\mathbf{x}\mathbf{N}_\mathbf{X}^{-1}$, where

$$\begin{aligned} \mathbf{N}_\mathbf{x} &= \begin{bmatrix} \mathbf{x}_1 - \mathbf{x}_4 & \mathbf{x}_2 - \mathbf{x}_4 & \mathbf{x}_3 - \mathbf{x}_4 \end{bmatrix} \\ \mathbf{N}_\mathbf{X} &= \begin{bmatrix} \mathbf{X}_1 - \mathbf{X}_4 & \mathbf{X}_2 - \mathbf{X}_4 & \mathbf{X}_3 - \mathbf{X}_4 \end{bmatrix} \end{aligned} \tag{12}$$

Using tetrahedral elements for 3D problems, $\mathbf{F}$ is 3×3 matrix and using triangle elements for 2D problems in the case of having a plane strain problem $\mathbf{F}$ would be a 2×2 matrix.

In general material models, Ψ is function of $\mathbf{E}$ or $\mathbf{F}$; However, for isotropic materials, Ψ is a function of the invariants of the right Cauchy–Green deformation tensor

$$\Psi = \Psi(\mathbf{I}_1, \mathbf{I}_2, \mathbf{I}_3) \tag{13}$$

where $\mathbf{I}_1 = \mathrm{tr}(\mathbf{C}), \mathbf{I}_2 = \frac{1}{2}\left[[\mathrm{tr}(\mathbf{C})]^2 - \mathrm{tr}\left(\mathbf{C}^2\right)\right]$, and $\mathbf{I}_3 = \det(\mathbf{C})$.

Several material models exist to describe the hyperelastic behaviour of tissue including Neo-Hookean, Ogden, Mooney-Rivlin, Arruda-Boyce [21]. The Neo-Hookean model is the most relevant, and most used, model for modelling breast tissue [22]. In this paper Neo-Hookean material model is used for modelling breast tissue. The strain energy function of a Neo-Hookean material is given by [23]

$$\Psi = \frac{\mu}{2}\left(\overline{\mathbf{I}_1} - 3\right) + \frac{\kappa}{2}(\mathbf{J}-1)^2 \tag{14}$$

where $\mathbf{J} = \frac{1}{2}\mathbf{I}_3$, $\overline{\mathbf{C}} = \mathbf{J}^{-2/3}\mathbf{C}$ and $\overline{\mathbf{I}_1} = \mathrm{tr}(\overline{\mathbf{C}})$. Material constants are $\mu = \frac{E}{2(1+\nu)}$, and $\kappa = \frac{E}{3(1-2\nu)}$, in which E is Young's modulus and ν is Poisson's ratio.

The strain energy of each element can be calculated using $\mathrm{U}_i = \Psi_i \mathrm{V}_i$, where V_i is the initial volume of the element and Ψ_i is the value of the strain energy density function measuring element's deformation. U_i is used in (10) to update $\mathbf{z}_i$ value for each element.

III. Control method

With the assumption that tissue deformation happens at low velocities, the problem can be considered as quasi-static, in which in each step the internal forces are in equilibrium with external forces. The set of control points on the tissue surface are denoted by $\mathbf{c}$ and the set of target points inside the tissue are denoted by $\mathbf{m}$.

A. Model Linearization

To calculate a linear relation between the displacement of control points $\delta\mathbf{x_c}$ and target points $\delta\mathbf{x_m}$, the Jacobian, we need to linearize the model around the current configuration. The quasi static equation of the system $\mathbf{F}_{\text{int}}(\mathbf{x_n}) = \mathbf{F}_{\text{ext}}$ is linearized using a Taylor series as $\mathbf{F}_{\text{int}}(\mathbf{x_n}) + \frac{\partial \mathbf{F}_{\text{int}}}{\partial \mathbf{x}}(\mathbf{x_{n+1}} - \mathbf{x_n}) = \mathbf{F}_{\text{ext}}(\mathbf{x_{n+1}})$, where $\mathbf{K} = \frac{\partial \mathbf{F}_{\text{int}}}{\partial \mathbf{x}}$ is the tangent stiffness matrix of the system. Having an applied variation in external forces, the variation in node positions can be calculated using $\delta\mathbf{x} = \mathbf{K}^{-1}\delta\mathbf{F}_{ext}$.

In order to derive Jacobian from a linearized static equation a modification in force vector representation is necessary,

$$\mathbf{F}_{\text{ext}} = \mathbf{J_c}\lambda \tag{15}$$

where λ is a vector including all nonzero values of external forces applied to system DoF (i.e., if the number of control points is c, and λ is a $c \times 1$ vector) and $\mathbf{J_c}$ is an $N \times c$ matrix consisting of zeros and ones which relates the vector λ to the global external force vector which is $N \times 1$. The relationship between the parameter variations such as $\delta\mathbf{x_m}$, $\delta\mathbf{x_c}$, and $\delta\mathbf{x}$ is defined as

$$\begin{aligned} \delta\mathbf{x_c} &= \mathbf{J_c}^T \delta\mathbf{x} \\ \delta\mathbf{x_m} &= \mathbf{J_m}^T \delta\mathbf{x} \end{aligned} \tag{16}$$

where $\mathbf{J_m}$ is a similar matrix to $\mathbf{J_c}$ that extracts target point variation from the vector of all node displacements, $\delta\mathbf{x}$. The relationship between $\delta\mathbf{x_c}$ and $\delta\mathbf{x_m}$ and force vector λ is given by

$$\begin{aligned} \delta\mathbf{x_c} &= \mathbf{J_c}^T \mathbf{K}^{-1} \mathbf{J_c}\lambda \\ \delta\mathbf{x_m} &= \mathbf{J_m}^T \mathbf{K}^{-1} \mathbf{J_c}\lambda \end{aligned} \tag{17}$$

By eliminating the force vector from two equations in (17), the final relationship is

$$\delta\mathbf{x_m} = \mathbf{J_m}^T \mathbf{K}^{-1} \mathbf{J_c}\left(\mathbf{J_c}^T \mathbf{K}^{-1} \mathbf{J_c}\right)^{-1} \delta\mathbf{x_c} \tag{18}$$

Therefore the Jacobian of the system is

$$\mathbf{J_s} = \mathbf{J_m}^T \mathbf{K}^{-1} \mathbf{J_c}\left(\mathbf{J_c}^T \mathbf{K}^{-1} \mathbf{J_c}\right)^{-1}. \tag{19}$$

The tangent stiffness matrix $\mathbf{K}$ is computed using the Rayleigh-Ritz method that states the first derivative of deformation, or strain energy function, with respect to current node positions gives the nodal force and second derivative gives the stiffness matrix; therefore, $\mathbf{K}_{ij} = \left(\frac{\partial^2 \mathbf{U}}{\partial \mathbf{x_j} \partial \mathbf{x_i}}\right)$. The standard method to calculate the global stiffness matrix of an element grid is to calculate local stiffness related to each element separately and then integrate the stiffness of all elements to obtain the global matrix. The local stiffness matrix associated with individual element follows the relationships $\mathbf{K_e} = \mathbf{V}_e\left(\frac{\partial^2 \Psi_e}{\partial \mathbf{x_j} \partial \mathbf{x_i}}\right)$. Having the strain energy function using (14) and gradient deformation matrix $\mathbf{F}$, the element local stiffness matrix is obtained by computing the matrix of second derivative of strain energy function with respect to element's node DoF as follows:

$$\begin{aligned} &\mathbf{K_e} = \mathbf{V}_e\left(\mathbf{N_e}\mathbf{D_X}^{-1} \otimes \mathbf{I_3}\right) \\ &\begin{bmatrix} \left(\frac{\mu}{3}\mathbf{J}^{-\frac{2}{3}}\mathbf{I_1} - \kappa\mathbf{J}(\mathbf{J}-\mathbf{1})\right)\mathbf{Q_{(n,n)}}^T\left(\mathbf{F}^{-T} \otimes \mathbf{F}^{-1}\right) + \\ \frac{\mu}{3}\mathbf{J}^{-\frac{2}{3}}\mathbf{I_3} \otimes \mathbf{I_3} - \frac{4\mu}{3}\mathbf{J}^{-\frac{2}{3}}\mathrm{vec}\left(\mathbf{F}^{-T}\right)\mathrm{vec}(\mathbf{F})^T \\ + \left(\frac{2\mu}{9}\mathbf{J}^{-\frac{2}{3}}\mathbf{I_1} - \kappa\mathbf{J}(\mathbf{2J}-\mathbf{1})\right)\mathrm{vec}\left(\mathbf{F}^{-T}\right)\mathrm{vec}\left(\mathbf{F}^{-T}\right)^T \end{bmatrix} \\ &\left(\mathbf{D_X}^{-T}\mathbf{N_e}^T \otimes \mathbf{I_3}\right) \end{aligned} \tag{20}$$

where $\mathbf{N_e} = \begin{bmatrix} 1 & 0 & 0 \\ 0 & 1 & 0 \\ 0 & 0 & 1 \\ -1 & -1 & -1 \end{bmatrix}$ for tetrahedral elements and $\mathbf{N_e} = \begin{bmatrix} 1 & 0 \\ 0 & 1 \\ -1 & -1 \end{bmatrix}$ for triangle elements. $\mathbf{Q_{(n,n)}}$ is a $n^2 \times n^2$ matrix that is partitioned by $n \times n$ blocks. Each block has the from $\mathbf{O_{ij}} = \left(\mathbf{o}_{s,t}^{(i,j)}\right)$ whose nonzero entry is $\mathbf{o}_{j,i}^{(i,j)} = 1$. The operator $\otimes$ is the Kronecker product and vec() operator vectorizes a matrix.

B. Control and Manipulation Analysis

The main aim of this controllability analysis is to define a desired direction vector on which the internal point will be moved. To create this direction vector, we must consider that only a positive combination of all actuator movement vectors is allowed (i.e., actuators can only push the breast). Under this assumption, we will show that the internal target is able to be moved along any arbitrary directions if and only if the target movement vector lays on the span of the actuators' movement vector.

The necessary mathematical definition of positive basis theory which is required is summarized as follows;

Definition 1: A positive combination of a set of vectors $[\mathbf{a}_1 \cdots \mathbf{a}_r] \in \mathbb{R}^n$ is a linear combination $\lambda_1 a_1 + \cdots + \lambda_r a_r$ with $\lambda_i \geqq 0$.

Definition 2: A *a positive span* or *convex cone* is the set of all positive combination of a finite set of vectors that $\mathbb{A} = \{\mathbf{a} \in \mathbb{R}^n : \mathbf{a} = \lambda_1\mathbf{a}_1 + \cdots + \lambda_r\mathbf{a}_r, \lambda_i \geq 0, i = 1,...,r\}$.

Definition 3: A set of finite vectors $[\mathbf{a}_1 \cdots \mathbf{a}_r]$ is *positively independent* if there is no vector $\mathbf{a}_i$ in the set such that it can be written as a positive combination of the others.

Definition 4: If all the vectors in set $[\mathbf{a}_1 \cdots \mathbf{a}_r]$ are *positively independent*, the set is a *frame* of cone $\mathbb{A}$. All vectors in the vector set are called the *positive basis*.

With linearly independent orthogonal bases, the number of linearly independent bases spanning the space $\mathbb{R}^n$ is unique;

however, with positive basis, the number of positive bases which can span $\mathbb{R}^n$ and be positively independent are not unique.

Theory 1: The minimum number of *positive basis* that span $\mathbb{R}^n$ is $r=n+1$ and the maximum number of *positive basis* that span $\mathbb{R}^n$ is $r=2n$. The former one is called *minimal positive bases* and the later one is called *maximal positive bases*.

Corollary 1: A positive representation of a vector $\mathbf{a}\in\mathbb{A}$ is unique in each frame that spans set $\mathbb{A}$.

If the internal point is moved with a distance d in any arbitrary direction, set $\mathbb{A}$ (the span of positive bases) should be a circle with radius d as shown in Fig. 2. In a planar movement the dimension of the vector set is $n=2$, so to have *positive bases* which spans the whole set $\mathbb{A}$ based on Theory 1, at least $n+1=3$ (*minimal positive bases*) and at most $2n=4$ (*maximal positive bases*) actuators are required. Vectors $e_i\in[1,2,3]$ or $e_i\in[1,2,\cdots 4]$ (see Fig. 2.) should be chosen such that they are *positively independant* to be capable of spanning set $\mathbb{A}$ entirely as shown in Fig. 2.

Based on Corollary 1, if the vectors are chosen such that they are *positively independant*, the representation of point p in Fig .2 is unique in both maximal and minimal configurations.

In order to choose between the minimal and maximal frame configurations, a manipulability index is introduced as

$$\text{Manipualbility Index} = \frac{\|p\|_2}{\sum_{i=1}^{n}\|q_i\|_2} \tag{21}$$

where $\|.\|_2$ is euclidean norm of vectors in the global Cartesian frame (Fig. 2), p is the target displacement vector, and q_i are the displacement vectors of the actuators represented in the global Cartesian frame.

The amount of tissue deformation is proportional to all of actuators' displacements. Larger actuator displacement means the tissue is deformed more. The manipulability index defines the ratio between target movement and actuators movement (i.e., tissue deformation). A larger manipulability index means less tissue deformation is applied to move the target for the same amount of displacement.

In order to obtain a manipulability index for each vector p, based on (21), each q_i needs to be calculated. Due to the definition of manipulability index, this is a task specific index. To calculate each actuator movement vector q_i, the following inverse kinematic problem under joint constraints is solved.

$$\begin{aligned} &\underset{\mathbf{q}}{\text{argmin}}\|p-\mathbf{J_s}q\| \\ &\text{s.t.} \quad q_i{d_i}^T\geq 0 \end{aligned} \tag{22}$$

where $\mathbf{J_s}$ is the Jacobian matrix for each configuration obtained using (19), and d_i is the acting direction of actuators. The above inverse kinematic problem is calculated for each actuator configurationand is shown in Fig. 2 with respect to three specific tasks:

1) Task 1: points inside the circle are moved by 5 mm along the negative direction of the x axis and their movement along the y axis is relaxed.
2) Task 2: points inside the circle are moved by 5 mm along the negative direction of the y axis and their movement along the x axis is relaxed.
3) Task 3: points inside the circle are moved by 5 mm along the positive direction of the y and the x axes simultaneously.

The task will be achieved through the control objective in section IV-B. The manipulability index distribution for minimal and maximal configuration is depicted in Fig .3. Based on Fig. 3, maximal configuration with 4 actuators has the larger manipulability index in the majority of area and it means that this actuator configuration is able to move the target with less tissue deformation.

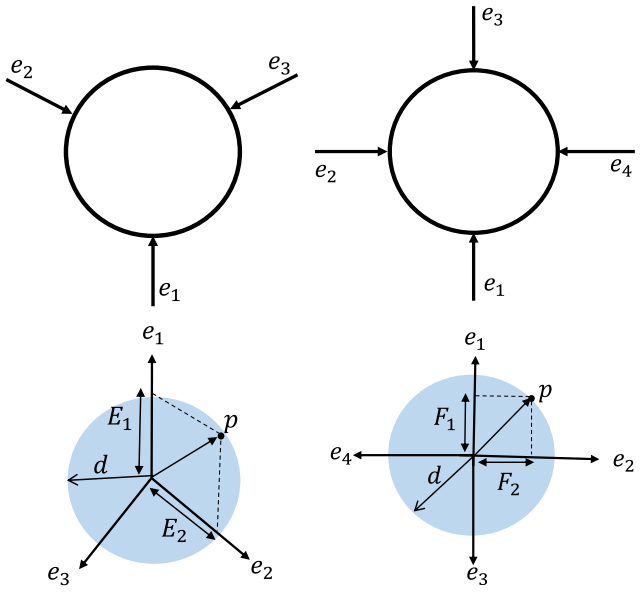

(a) Minimal positive bases. (b) Maximal positive bases.

Fig. 2: Positive bases and positive spanned area.

C. MPC Controller

In this section, a Model Predictive Control (MPC) scheme is designed. MPC is selected because of its ability to constrain the magnitude and direction of the control effort, to control MIMO systems in a standard state-space formulation, and also its ability to eliminate steady-state error. As explained in Section III-A, the simulated model of the system is linearized at each step. Using the linearized system, a multivariable MPC controller is designed to compute the optimal displacement of boundary points such that actuators only push the tissue and, in addition, they are not able to retract. The linearized system can be reformulated into a state-space formulation as follows

$$\begin{aligned} \mathbf{x_m}(k+1) &= \mathbf{x_m}(k)+\mathbf{J_s}(\mathbf{x_m}(k),\mathbf{x_r}(k))\,\mathbf{u}(k) \\ \mathbf{y}(k) &= \mathbf{x_m}(k) \end{aligned} \tag{23}$$

Here, the system states consist of the position of the target point $\mathbf{x}_m$ and $\mathbf{u}=\delta\mathbf{x_c}$ is the displacement variation of the boundary points, which are the control inputs. The control input matrix (i.e., the Jacobian) is a parameter varying matrix that depends on both the current states of the system and also the position of all other nodes within the model $\mathbf{x_r}$. Vector $\mathbf{y}$ is the measurement vector which is the position of target point $\mathbf{x_m}$.

The objective of MPC is to compute a series of discrete optimal control inputs using the predicted future states of a system in each optimization horizon to minimize the cost function and satisfy the constraints. The error signal between the defined reference set point and predictive position of the target from the linear model is obtained as

$$\mathbf{e}(k+h)=\mathbf{y}_\mathrm{d}(k+h)-\mathbf{y}_\mathrm{p}(k+h) \tag{24}$$

where $\mathbf{y}_\mathrm{p}$ is the predicted target location obtained using (23). The quadratic constrained optimization problem is

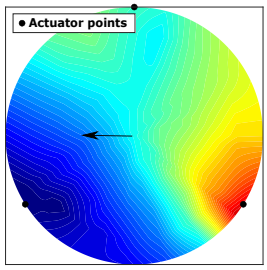

(a) The three-actuator configuration, task one

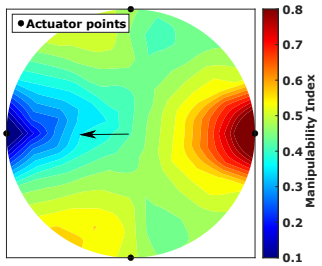

(b) The four-actuator configuration, task one.

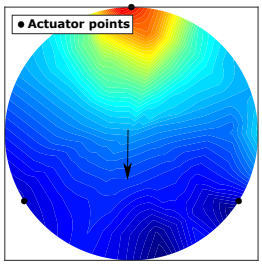

(c) The three-actuator configuration, task two.

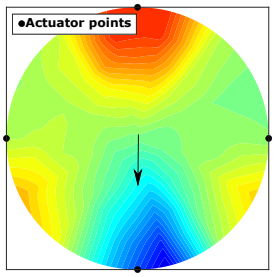

(d) The four-actuator configuration, task two.

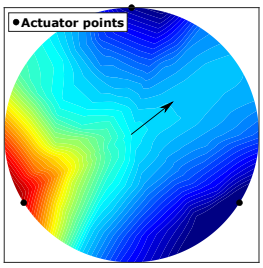

(e) The three-actuator configuration, task three.

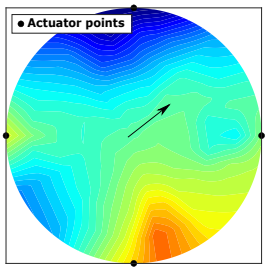

(f) The four-actuator configuration, task three.

Fig. 3: Manipulability distribution maps (The black arrows show the movement direction of internal points at each task).

$$\begin{aligned} \mathscr{J} &= \min \frac{1}{2}\sum_{h=0}^{N_p}\left[\mathbf{e}^T\mathbf{Q}\mathbf{e}+\mathbf{u}^T\mathbf{R}\mathbf{u}\right] \\ &\text{s.t.} \\ &\mathbf{x_m}(k+1)=\mathbf{x_m}(k)+\mathbf{J_s}(\mathbf{x_m}(k),\mathbf{x_r}(k))\,\mathbf{u}(k) \\ &\mathbf{y}(k)=\mathbf{x_m}(k) \\ &\mathbf{u_i}\mathbf{d_i}^T\geq 0 \end{aligned} \tag{25}$$

where $\mathbf{u_i}$ is the actuator displacement of each actuator, and $\mathbf{d_i}$ is the acting direction of actuators. $\mathbf{Q}$ and $\mathbf{R}$ are square weighting matrices. N_p is the prediction horizon. The system's actuators are constrained to only move forward based on (25). A block diagram of the MPC control procedure is shown in Fig. 4.

IV. Simulation and Experimental Results

In this section, the accuracy of the minimum-energy-based method is compared with experimental data. The performance of the MPC controller is also evaluated through experiments.

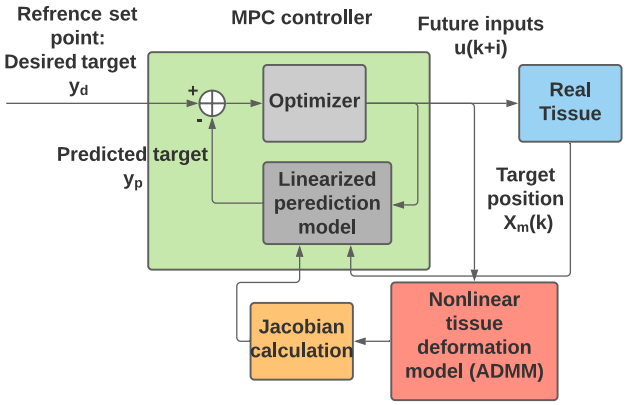

Fig. 4: Block diagram of the MPC controller. The outputs are the inner target point positions, the inputs are the displacements of the control boundary points, and the system states are the position of the system's DoFs at each configuration.

A. Model Validation in Phantom Tissue

To experimentally validate the performance of the proposed method in tissue deformation prediction, an experimental setup (Fig. 5) was built. An Aurora electromagnetic (EM) tracker with a Planar 20-20 V2 Field Generator (NDI Europe GmbH, Radolfzell, Germany) is utilized to track the 3D position of a magnetic sensor which was located inside the tissue phantom at five different target points as shown in Fig. 5. Four linear actuators displaced the tissue boundary in discrete steps of $\{5,10,15\}mm$ (i.e. 12 experiments have been done for each internal point separately). A tissue phantom made from plastisol and softener (M-F Manufacturing Co, Fort Worth, USA) with an equal volume ratio. The module of elasticity of the phantom that is calculated through compression test is $E=6kPa$.

Five internal targets are considered inside the tissue for the model verification experiments. The experimental layout of phantom, actuators, and targets is shown in Fig. 6. The top view of targets and actuators is displayed in Fig. 6a and Fig. 6b shows a 3D view of actuators and targets' arrangements.

The mesh model of the breast in Fig. 6, which is used for simulation has been built based on the CAD model and the Tetgen library is used to mesh the CAD model in MATLAB. The minimum-energy-based method was programmed in C++ using OpenMP, and it was run on an Intel® Core™ i5 processor with 6 cores. The total computation time for the 800 iterations and 1706 tetrahedral elements is 15 seconds. The speed can further be improved by implementing the algorithm on a GPU. The location of the five internal target points, induced by boundary displacement, were measured and the mean, median and standard deviation of square error between the simulation and experiment results for the five target points in X, Y, and Z directions were calculated and are shown in Fig. 7. For each target, experimental studies for 12 trials were conducted. There are red lines indicating the median error, blue boxes indicating the 25th and 75th percentile, whiskers indicating the minimum and maximum error, and an orange circle indicating the mean error. The maximum target localization error is on the order of 1.6 mm showing that the minimum-energy-based method is highly accurate with respect to real tissue deformation.

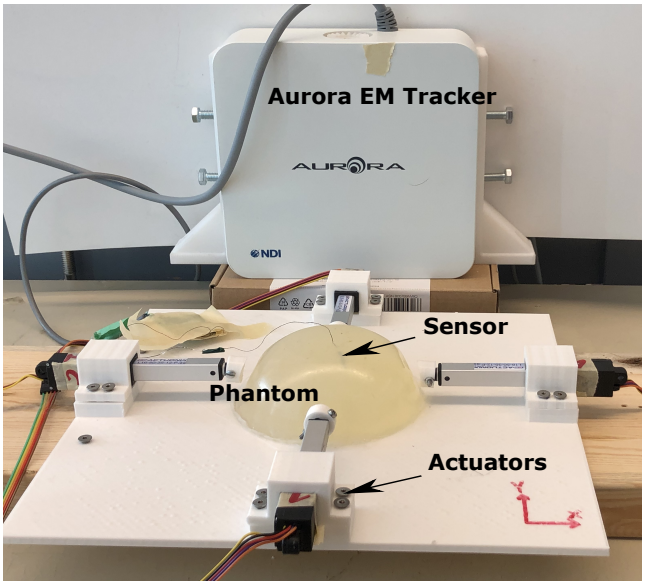

Fig. 5: Experiment setup. An Aurora electromagnetic (EM) tracker is used to track the 3D position of targets. Linear actuators push the tissue phantom made of plastisol.

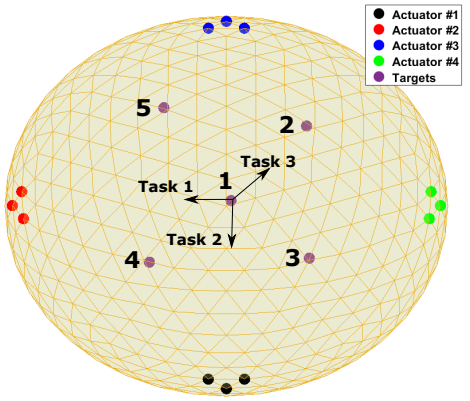

(a) The top view.

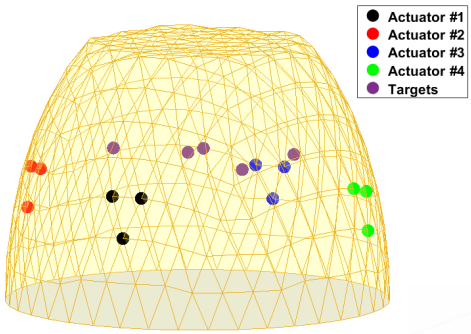

(b) The 3D view.

Fig. 6: The layout of breast phantom, actuators, targets, and tasks. a) shows the top view of the layout and b) shows the 3D view of the layout.

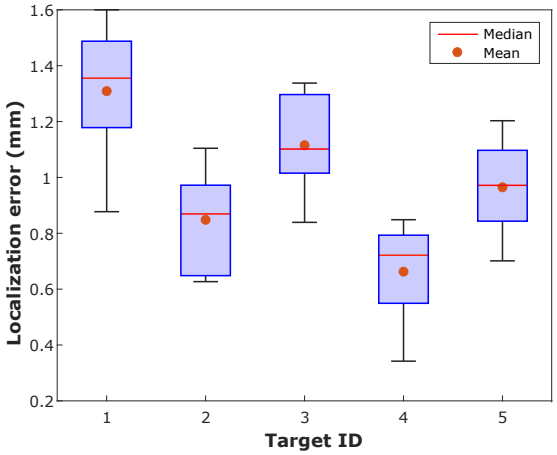

Fig. 7: Localization error for five targets between the experimental and simulation data.

B. Control Loop Validation

The defined task in Section III-B, are carried out on two different points, points 1 and 2 shown in Fig. 6. The MPC controller parameters are $N_p = 5$, $Q = 3I_{2\times2}$, and $R = 2I_{4\times4}$. The weighting matrices have been defined experimentally to make sure the convergence is fast while avoiding any sudden jump in actuator movements.

Fig. 8, Fig. 9 and Fig. 10 show the results for point 1 and Fig. 11, Fig. 12 and Fig. 13 illustrate the results for point 2. In the first part of the presented figures, the results from open loop scheme is presented by red curve and the experimental result (closed-loop) is demonstrated by blue curve. Also, the green line shows the desired position. In the second part, the actuators movements are shown. It is noteworthy that retraction of actuators is not allowed in this method. In Fig. 8 and Fig. 9 only one actuator moves to displace point 1 based on task one and two, respectively. The closed loop scheme is able to reach the desired location after 80 s in Fig. 8 while in Fig. 9, the experimental result reaches the desired position after 60 s. As can be seen in both cases, in the initial steps the actuator moves the most distance, and as time passes the actuator displacement reduces. In Fig. 10, two actuators are activated to move point 1 to the desired location based on task three.

To show that the proposed scheme is effective in every other points, the same studies are conducted on point 2, where in Fig. 11, Fig. 12, one actuator displaces the phantom along task one and task two respectively to reach the desired location. For both of these studies, it takes 80 s for the closed-loop controller to get to desired position. In Fig. 13, two actuators are used to move the target point along task three. The results converged after 80 s. As it is shown in these figures, the MPC structure with state feedback is robust to slight simulation position error in the open-loop simulations and the Jacobian calculated based on the minimum-energy-based simulation results is a good approximation of the relation between boundary points displacements and internal target displacement.

In Table I, the defined tasks are carried out on points 1, 2, 3, ,4 and 5, and the integral of absolute error (AITE),

$$ITAE = \int t|\varepsilon|dt, \tag{26}$$

is used as a measure of control system performance to do the comparison between the open-loop and closed-loop performance.

As can be seen, the error in all the points and tasks is reduced in the closed-loop scheme.

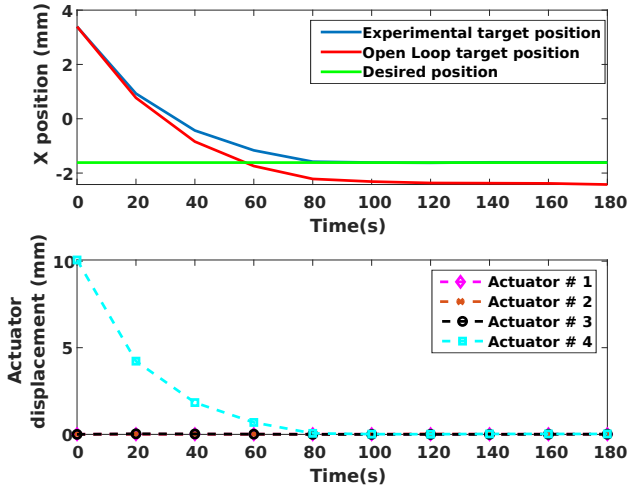

Fig. 8: The time response of the target point 1 position and actuators' movement for task one.

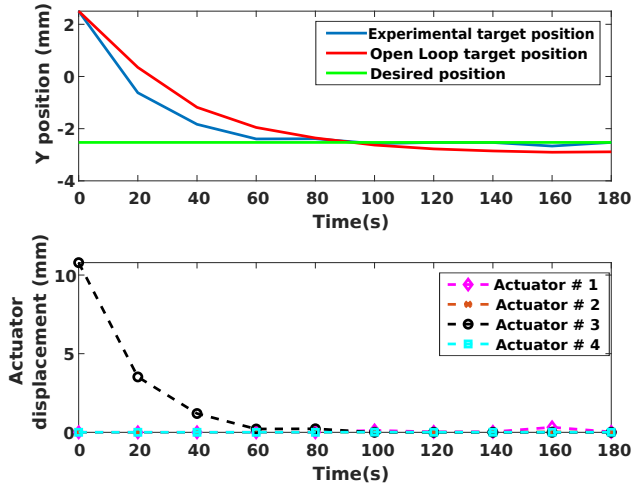

Fig. 9: The time response of the target point 1 position and actuators' movement for task two.

V. Conclusion

An innovative model-based control method was presented in this study for implementing multi-point tissue manipulation in order to position a target in line with the brachytherapy needle in breast brachytherapy.

To this end, a model predictive controller (MPC) was designed using an online linear approximation of the biomechanical model of tissue at each time step, which moves a target point (inside of tissue) to the desired location. The performance of the proposed method was demonstrated through experiments on the tissue phantom. Experimental results demonstrate that MPC successfully converges to the desired location without a substantial steady-state error and AITE index of closed-loop is much less that open-loop simulation. The open-loop simulation has a steady state error in the range of 2 mm.

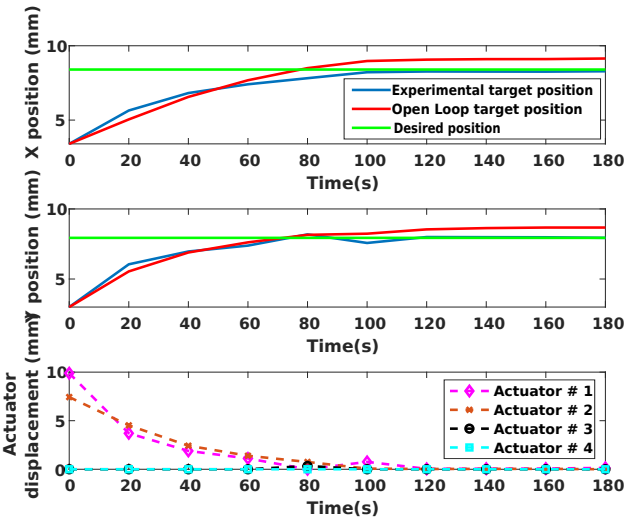

Fig. 10: The time response of the target point 1 position and actuators' movement for task three.

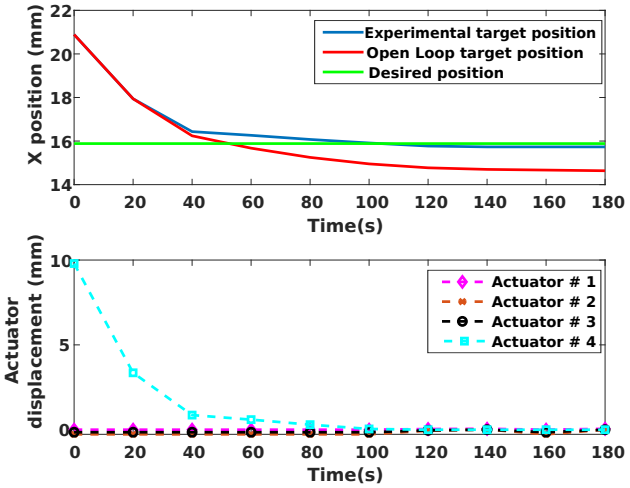

Fig. 11: The time response of the target point 2 position and actuators' movement for task one.

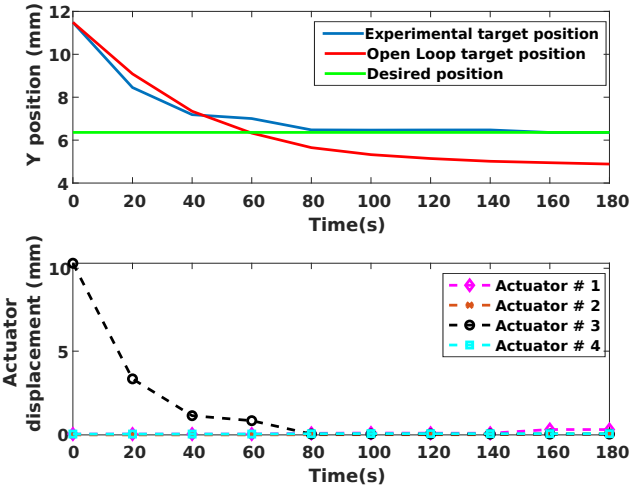

Fig. 12: The time response of the target point 2 position and actuators' movement for task two.

TABLE I: AITE index and steady-state error for closed-loop and open-loop results.

Target ID	Scenarios	Open loop AITE	Closed loop AITE	Open loop steady-state error (mm)
1	Task 1	403.40	193.23	0.66
	Task 2	342.52	117.22	0.36
	Task 3	910.17	231.02	0.92
2	Task 1	1172.6	155.61	1.64
	Task 2	1046.8	144.67	1.47
	Task 3	931.33	260.22	1.35
3	Task 1	1201.12	604.45	2.42
	Task 2	752.62	171.21	0.46
	Task 3	1319.85	297.01	1.88
4	Task 1	1112.89	285.3	1.37
	Task 2	986.23	195.67	1.12
	Task 3	1360.5	521.61	1.93
5	Task 1	1036.10	350.21	2.1
	Task 2	1205.37	270.9	1.4
	Task 3	1112.34	130.71	1.61

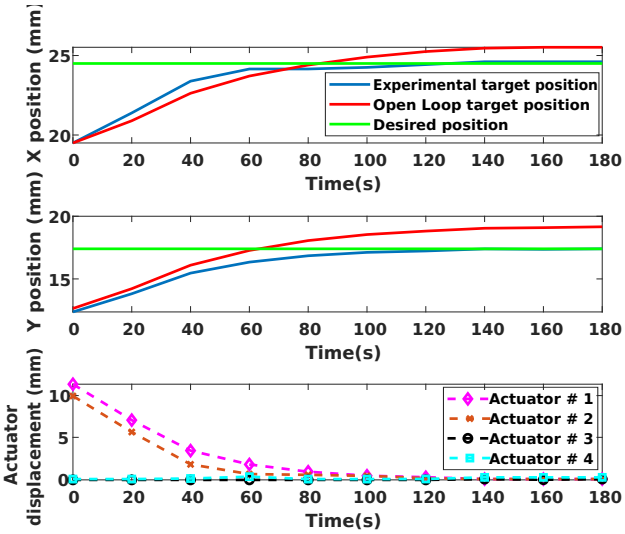

Fig. 13: The time response of the target point 2 position and actuators' movement for task three.

To simulate non-linear tissue deformation, the dynamics of soft tissue were turned into a parallelizable optimization problem, where the deformed tissue strain energy is considered part of the cost function required to be optimized. The capability of the solver to be parallelized, makes it a suitable choice to be used in a real-time control method. The accuracy of the proposed solver was evaluated through a comparison in phantom tissue experimental results, showing the model has an error of 1.6 mm with respect to real-world tissue. The sufficient number of actuators was found through a controllability analysis. Based on the theory of positive basis sets, actuator configurations with three and four actuators guarantee the controllability of the target in a 2D plane. The configuration with four actuators, however, imposes less tissue deformation for the same target movement and hence this configuration was chosen in this work.

Currently, MPC converges under the condition of having a direct measurement of the internal target. It is possible to track the position of the internal target through US image frames; however, it is not a trivial task. For future work, an observer will be designed based on the biomechanical model and data from the surface point to calculate the position of the internal target without having a sensor inside the tissue.

REFERENCES

[1] G. Wan, Z. Wei, L. Gardi, D. B. Downey, and A. Fenster, "Brachytherapy needle deflection evaluation and correction," *Medical physics*, vol. 32, no. 4, pp. 902–909, 2005.

[2] E. E. Deurloo, K. G. Gilhuijs, L. J. S. Kool, and S. H. Muller, "Displacement of breast tissue and needle deviations during stereotactic procedures," *Investigative radiology*, vol. 36, no. 6, pp. 347–353, 2001.

[3] J. op den Buijs, M. Abayazid, C. L. de Korte, and S. Misra, "Target motion predictions for pre-operative planning during needle-based interventions," in *2011 Annual International Conference of the IEEE Engineering in Medicine and Biology Society*. IEEE, pp. 5380–5385.

[4] R. E. S. R. E. H. Q. W. Pignol JP, Keller B, "First report of a permanent breast 103pd seed implant as adjuvant radiation treatment for early-stage breast cancer." *nt J Radiat Oncol Biol Phys*, 2006.

[5] C. Rossa and M. Tavakoli, "Issues in closed-loop needle steering," *Control Engineering Practice*, vol. 62, pp. 55–69, 2017.

[6] M. Khadem, C. Rossa, N. Usmani, R. S. Sloboda, and M. Tavakoli, "Robotic-assisted needle steering around anatomical obstacles using notched steerable needles," *IEEE journal of biomedical and health informatics*, vol. 22, no. 6, pp. 1917–1928, 2017.

[7] M. Torabi, K. Hauser, R. Alterovitz, V. Duindam, and K. Goldberg, "Guiding medical needles using single-point tissue manipulation," in *2009 IEEE International Conference on Robotics and Automation*. IEEE, 2009, pp. 2705–2710.

[8] E. Coevoet, A. Escande, and C. Duriez, "Optimization-based inverse model of soft robots with contact handling," *IEEE Robotics and Automation Letters*, vol. 2, no. 3, pp. 1413–1419, 2017.

[9] P. Baksic, H. Courtecuisse, C. Duriez, and B. Bayle, "Robotic needle insertion in moving soft tissues using constraint-based inverse finite element simulation," in *2020 IEEE International Conference on Robotics and Automation (ICRA)*. IEEE, 2020, pp. 2407–2413.

[10] W. Zhang, Y. Zhang, and Y. Liu, "Design and control of a bionic needle puncture robot," *The International Journal of Medical Robotics and Computer Assisted Surgery*, vol. 17, no. 2, p. e2200, 2021.

[11] V. G. Mallapragada, N. Sarkar, and T. K. Podder, "Robot-assisted real-time tumor manipulation for breast biopsy," *IEEE Transactions on Robotics*, vol. 25, no. 2, pp. 316–324, 2009.

[12] R. Lagneau, A. Krupa, and M. Marchal, "Active deformation through visual servoing of soft objects," in *ICRA 2020-IEEE International Conference on Robotics and Automation*, 2020.

[13] F. Alambeigi, Z. Wang, R. Hegeman, Y.-H. Liu, and M. Armand, "A robust data-driven approach for online learning and manipulation of unmodeled 3-d heterogeneous compliant objects," *IEEE Robotics and Automation Letters*, vol. 3, no. 4, pp. 4140–4147, 2018.

[14] Z. Wang, X. Li, D. Navarro-Alarcon, and Y.-h. Liu, "A unified controller for region-reaching and deforming of soft objects," in *2018 IEEE/RSJ International Conference on Intelligent Robots and Systems (IROS)*, 2018, pp. 472–478.

[15] J. Zhang, Y. Zhong, and C. Gu, "Deformable models for surgical simulation: a survey," *IEEE reviews in biomedical engineering*, vol. 11, pp. 143–164, 2017.

[16] N. Lauzeral, D. Borzacchiello, M. Kugler, D. George, Y. Rémond, A. Hostettler, and F. Chinesta, "A model order reduction approach to create patient-specific mechanical models of human liver in computational medicine applications," *Computer methods and programs in biomedicine*, vol. 170, pp. 95–106, 2019.

[17] Y. Duan, W. Huang, H. Chang, W. Chen, J. Zhou, S. K. Teo, Y. Su, C. K. Chui, and S. Chang, "Volume preserved mass–spring model with novel constraints for soft tissue deformation," *IEEE journal of biomedical and health informatics*, vol. 20, no. 1, pp. 268–280, 2014.

[18] I. Berndt, R. Torchelsen, and A. Maciel, "Efficient surgical cutting with position-based dynamics," *IEEE computer graphics and applications*, vol. 37, no. 3, pp. 24–31, 2017.

[19] E. Tagliabue, D. Dall'Alba, E. Magnabosco, C. Tenga, I. Peterlík, and P. Fiorini, "Position-based modeling of lesion displacement in ultrasound-guided breast biopsy," *International journal of computer assisted radiology and surgery*, vol. 14, no. 8, pp. 1329–1339, 2019.

[20] M. Overby, G. E. Brown, J. Li, and R. Narain, "Admm : Projective dynamics: Fast simulation of hyperelastic models with dynamic constraints," *IEEE Transactions on Visualization and Computer Graphics*, vol. 23, no. 10, pp. 2222–2234, 2017.

[21] E. W. Chaves, *Notes on continuum mechanics*. Springer Science & Business Media, 2013.

[22] A. Samani, J. Zubovits, and D. Plewes, "Elastic moduli of normal and pathological human breast tissues: an inversion-technique-based investigation of 169 samples," *Physics in medicine & biology*, vol. 52, no. 6, p. 1565, 2007.

[23] J. Bonet and R. D. Wood, *Nonlinear continuum mechanics for finite element analysis*. Cambridge university press, 1997.

Mehrnoosh Afshar received the BSc degree in mechanical engineering from Amirkabir University of Technology (Tehran Polytechnic) in 2014 and the MSc degree in mechanical engineering from the Sharif University of Technology in 2016. She is currently pursuing a Ph.D. in Electrical Engineering at the University of Alberta. Her research interests involve mechanical design, modeling and application of theory of control in medical application. Currently, she focuses on developing systems for Robot-assisted breast brachytherapy.

Jay Carriere earned his B.Sc. in Electrical Engineering and Ph.D. in Biomedical Engineering from the University of Alberta in 2011 and 2019, respectively. Between his B.Sc. and Ph.D. studies, he worked in industry as a project engineer gaining experience in controls, instrumentation, and fabrication. He is currently an Assistant Professor at the University of Calgary in the Department of Electrical and Software Engineering. His current interdisciplinary research is based around control systems and theory for human-robot interaction, specifically assistive, collaborative, and medical and surgical robotics. His research interests include areas such as intelligent control, computer vision, impedance control, mechatronics, and machine learning technologies.

Tyler Meyer Meyer is now a medical physicist at the Tom Baker Cancer Centre in Calgary. He is also an adjunct associate professor at the U of C in the department of oncology, with a secondary appointment in the department of physics and astronomy. The primary focus of his research and clinical practice is brachytherapy, a classification of radiotherapy where radioactive seeds or sources are placed in or near the target area. It's commonly used in cancer treatment for prostate, cervical and other gynecological cancers. But Meyer is also doing groundbreaking research on breast brachytherapy.

Ron S.Sloboda received the B.Sc. degree in physics from the University of Manitoba, Winnipeg, MB, Canada, in 1974, and the Ph.D. degree in physics, nuclear theory, from the University of Alberta, Edmonton, AB, Canada, in 1979. He is currently a Professor in the Department of Oncology, University of Alberta. His research interests include dosimetry and treatment planning for brachytherapy, including the design of clinical studies to obtain patient data and model based dose calculation.

Nawaid Usmani main focus on research is in prostate brachytherapy. Dr. Usmani's main objective for this research is to characterize current brachytherapy techniques and identify strategies for improving this treatment. In addition to this research in prostate brachytherapy, Dr. Usmani is involved in a number of other research endeavours. His other research includes: Investigating the potential benefits of metformin in preventing metabolic complications of hormonal therapy and improving prostate cancer outcomes; Identifying new prognostic or predictive biomarkers in prostate cancer; Investigating the utility of magnetic resonant imaging and PET imaging in the management of prostate cancer; and Investigating the potential benefits of exercise in rectal cancer patients.

Siraj Hussain Husain completed medical school at the Dalhousie University (Halifax, Nova Scotia) followed by residency training at the University of Alberta (Edmonton, Alberta). He completed a fellowship in Radiation Oncology at the University of Western Ontario (London, Ontario). His current clinical areas of focus include genitourinary and breast cancer. He has clinical and research interests in Brachytherapy and leads the implementation and training of HDR to new physicians at the Tom Baker Cancer Centre (TBCC). Dr. Husain is the Clinical and Research Program Leader for Prostate Brachytherapy, Radiation Oncology, at the TBCC. Active areas of research include enhancement and progression of combined modality therapy (Prostate Brachy + External Beam Radiation Therapy), champion for intermediate and high risk prostate cancer "drafted protocol" for introduction of High Dose Rate (HDR) and research, continue to advocate for Breast Brachytherapy – with new research project to enhance and improve the procedure.

Mahdi Tavakoli is a Professor in the Department of Electrical and Computer Engineering, University of Alberta, Canada. He received his BSc and MSc degrees in Electrical Engineering from Ferdowsi University and K.N. Toosi University, Iran, in 1996 and 1999, respectively. He received his PhD degree in Electrical and Computer Engineering from the University of Western Ontario, Canada, in 2005. In 2006, he was a post-doctoral researcher at Canadian Surgical Technologies and Advanced Robotics (CSTAR), Canada. In 2007-2008, he was an NSERC Post-Doctoral Fellow at Harvard University, USA. Dr. Tavakoli's research interests broadly involve the areas of robotics and systems control. Specifically, his research focuses on haptics and teleoperation control, medical robotics, and image-guided surgery. Dr. Tavakoli is the lead author of Haptics for Teleoperated Surgical Robotic Systems (World Scientific, 2008). He is a Senior Member of IEEE and an Associate Editor for IEEE/ASME Transactions on Mechatronics, Journal of Medical Robotics Research, IET Control Theory Applications, IEEE Robotics and Automation Letters and Mechatronics.